Pergamon

Int. J. Solids Structures Vol. 35, Nos 34–35, pp. 4981–4997, 1998

Printed in Great Britain
0020–7683/98/$—see front matter

PII: S0020–7683(98)00105–X

ON THE CALCULATION OF BONE PORE WATER PRESSURE DUE TO MECHANICAL LOADING

DAJUN ZHANG, SHELDON WEINBAUM and STEPHEN C. COWIN†

The Center for Biomedical Engineering, CUNY Graduate School and Department of Mechanical Engineering, School of Engineering, City College of New York, New York, NY 10031, U.S.A.

(*Received* 30 *May* 1997; *in revised form* 30 *September* 1997)

Abstract—The purpose of this paper is to calculate the bone fluid pressure in the lacunar–canalicular porosity of the cortical bone matrix induced by functional mechanical loading and compare it with that induced by the blood pressure differences. This problem reduces to the problem of determining the bone fluid pressure in a representative axially compressed osteon which is approximately an annular cylindrical structure. Two available poroelastic approximations, a beam analogy model and a single osteon model, are compared and discussed. We find that: (1) at the lacunar–canalicular porosity of a typical load-carrying long bone, normal physiological loading induces a bone fluid pressure that is at least 40 times larger than that induced by the blood pressure differences; (2) the solutions of the beam analogy model and the single osteon model approach each other as the exterior-to-interior radius ratio of the osteon approaches one.

INTRODUCTION

We may say that the earth has a spirit of growth, and that its flesh is the soil; its bones are the successive strata of the rocks; ... its cartilage is the tufa stone; its blood the veins of its waters. From the *Codex Leicester*, Leonardo Da Vinci.

A mature cortical bone matrix has a lamellar structure. These lamellae are arranged in either parallel shape or closely-adjoined concentric shape. Each multilayered concentric cylinder is called an osteon, or a Haversian system. An average osteon is about 250 μm in exterior diameter, 50 μm in interior diameter, and 5 mm in length. Sections of cortical bone that are made from parallel lamellae are called lamellar bone, and those from osteons are called osteonal bone, which occupy most of the cortical volume. Each osteon is a structural entity, and its exterior boundary is often called the cement line. Each osteon has a central lumen that may house blood vessels and nerve fibers.

Compared with the lifeless rock, live cortical (compact) bone is a much more dynamic structure since it is under constant remodeling. It is thoroughly vascularized, innervated, and cell proliferated. The seemingly very dense matrix of the cortical (compact) bone actually has several levels of porosity associated with it that are filled with fluid. Generally speaking, these levels can be categorized, in descending orders of lengthscale, into (1) vascular level; (2) lacunar–canalicular level; and (3) mineral crystal level. The vascular level is associated with the channel spaces that accommodate the blood vessel network (and the usually concurrent neural network) in the bone matrix (Haversian canals and Volkmann's canals). These channels have a characteristic diameter of about 50 μm (varying from 50–170 μm, Atkinson and Hallsworth, 1982; Cooper *et al.*, 1966). The lacunar–canalicular level is associated with the labyrinth spaces that accommodate the bone cell network in the bone matrix. A lacuna is the roughly ellipsoidal space (about 8 μm long axis, 4 μm short axis) that houses an osteocyte body, and a canaliculus is the microtubular space (0.1–0.35 μm diameter, Atkinson and Hallsworth, 1982) that houses one of the many thin osteocytic processes protruding from their main osteocyte body. Processes from

† Author to whom correspondence should be addressed. Tel.: 001 212 650 5208. Fax: 001 212 787 3757. E-mail: scccc@cunyvm.cuny.edu

neighboring osteocytes connect to each other through gap junctions to form a cellular network. On the lowest mineral crystal level, in the mineralizing process of the bone matrix the miniature crystalized mineral fronts push into micropores that were originally occupied by bone fluid. The left-over fluid spaces (generally thought to be connected) mingled with the mineral micro-crystals and collagen fibers, etc., provide the lowest porosity. Depending on the extent of mineralization, the size of these micropores can vary from 10–300 Å (Holmes *et al.*, 1964).

Load-enhanced fluid movement within and between these three levels of porosity are very important to bone biology proper and to the mineral metabolism of the whole body. However, due to the structural difficulties involved with live bone experiments, many basic questions about the fluid movement in bone are still in debate. For example, it is still not clear to what extent the bone fluid at the mineral crystal level is free to move. Neuman and Neuman (1958) suggested that the fluid there is largely bound to the matrix and not likely to be driven to move by external loading, which means that it can be treated as a fixed constituent of the solid matrix. (However, since the fluid phase there is continuous, it may accommodate diffusion within it.) On the other hand, the vascular level porosity is most likely a very low pressure system, with a typical capillary pressure ranging from 15–60 mmHg (Brookes, 1971). The external loading would not have very much effect on its bulk amplitude since the load-driven pressure change there will relax almost immediately due to its large pore size and its connection to the medullary canal. The only physiologically important load-induced fluid pressure change will be at the lacunar–canalicular level. Load-induced fluid movement (driven by the load-induced fluid pressure gradient) is in direct contact with the osteocytes, hence is essential to the functioning of them. For example, it is our premise that the load-induced weak electrical potential (streaming potential, about 1.0 mV across the annular thickness of an osteon, Starkebaum *et al.*, 1979) is due to the movement of the electrolytic bone fluid relative to the charged solid–fluid interface in the lacunar–canalicular space.

The purpose of this paper is to calculate the load-induced bone fluid pressure at the lacunar–canalicular level, using poroelasticity theory (Biot theory, Rice and Cleary, 1976). Under either axial loading or bending, each osteon will experience an axial compression or tension due to its small size. Hence our problem is reduced to calculating the fluid pressure in a representative osteon under axial loading.

POROELASTICITY

Constitutive relations

The Rice–Cleary form of constitutive relations for poroelasticity are (Rice and Cleary, 1976),

$$2GE_{ij} = T_{ij} - \frac{\nu}{1+\nu} T_{kk}\delta_{ij} + \frac{3(\nu_u - \nu)}{B(1+\nu)(1+\nu_u)} p\delta_{ij}, \tag{1}$$

$$\chi - \chi_0 = \frac{3\rho_0(\nu_u - \nu)}{2GB(1+\nu)(1+\nu_u)}\left(T_{kk} + \frac{3}{B}p\right). \tag{2}$$

There are four material constants in the above constitutive equations: G, ν, B, and ν_u. G and ν are, respectively, the shear modulus and Poisson's ratio when the medium is deformed under the "drained" condition, i.e., when the medium is deformed while maintaining a constant pore fluid pressure. The opposite case is the "undrained" deformation which corresponds to the case when there is no fluid transport between the elements of the medium (e.g., when the time scale of the loading is too small), $\Delta\chi = 0$. The compressibility coefficient B and the undrained Poisson's ratio ν_u are defined in terms of the material properties by

$$B = \frac{1/K - 1/K_s}{v_0/K_f + 1/K - (1+v_0)/K_s}, \tag{3}$$

$$v_u = \frac{3v + B(1-2v)(1-K/K_s)}{3 - B(1-2v)(1-K/K_s)}, \tag{4}$$

where K is the "drained" bulk modulus $K = 2G(1+v)/3(1-2v)$, K_f is the bulk modulus of the fluid where we have set K_s, K_s', and K_s'' of Rice and Cleary (1976) equal, with no loss of generality to our formulation and solution.

The stress–strain relations (1) can also be written as

$$T_{ij} = 2GE_{ij} + \left(K - \frac{2G}{3}\right)\delta_{ij}E_{kk} - \zeta p\delta_{ij}, \tag{5}$$

where (cf e.g., Rudnicki, 1985)

$$\zeta = \frac{3(v_u - v)}{B(1-2v)(1+v_u)} = 1 - \frac{K}{K_s}. \tag{6}$$

Field equations

D'Arcy's law is written in the form

$$u_i = -\rho_0 \kappa\, \partial p/\partial x_i, \tag{7}$$

where u_i is the fluid mass flow rate per unit area in the x_i direction, κ is the permeability and $\kappa = k/\mu$ where μ (Pa s) is the viscosity of the fluid and k (m^2) is the specific permeability.

The stress/pore fluid pressure conditions of compatibility are given by Rice and Cleary (1976),

$$\nabla^2[(1+v)T_{ij} - vT_{kk}\delta_{ij}] + \partial^2 T_{kk}/\partial x_i\,\partial x_j + \frac{3(v_u - v)}{B(1+v_u)}[\nabla^2 p\delta_{ij} + \partial^2 p/\partial x_i\,\partial x_j] = 0. \tag{8}$$

A useful relation between T_{kk} and p is obtained by contracting eqn (8), thus

$$\nabla^2(T_{kk} + \Lambda p) = 0, \tag{9}$$

where

$$\Lambda = \frac{6(v_u - v)}{B(1-v)(1+v_u)} = \frac{2(1-2v)}{(1-v)}\zeta. \tag{10}$$

Another relation between T_{kk} and p can be obtained from the fluid mass conservation equation $\partial u_i/\partial x_i + \partial\zeta/\partial t = 0$, which yields

$$c\nabla^2\left(T_{kk} + \frac{3}{B}p\right) = \frac{\partial}{\partial t}\left(T_{kk} + \frac{3}{B}p\right), \tag{11}$$

where

$$c = \kappa\left[\frac{2G(1-v)}{(1-2v)}\right]\left[\frac{B^2(1+v_u)^2(1-2v)}{9(1-v_u)(v_u - v)}\right]. \tag{12}$$

Equations (8) and (11) constitute a set of seven coupled equations for the seven scalar

unknowns T_{ij} and p. These equations are those used in Zhang and Cowin (1994) to solve the problem of a poroelastic beam under combined oscillatory axial compression and bending.

FORMULATION

Beam solution

The formulation and an analytical solution for a poroelastic beam (Fig. 1), under a combined loading of an oscillatory axial force $N_z = N_0 \sin \omega t$ and an oscillatory bending moment $M_z = M_0 \sin \omega t$, have been given by Zhang and Cowin (1994). In this paper the evaluation of the various poroelastic material constants for the cortical bone at the lacunar–canalicular level given in Zhang and Cowin (1994) will be employed. The non-dimensionalization (cf Fig. 1) is,

$$Y \equiv \frac{y}{d}, \quad \tau \equiv \frac{ct}{d^2}, \quad T \equiv \frac{\omega d^2}{c}, \quad m \equiv \frac{3M_0}{N_0 d}, \quad P(\tau, Y) \equiv \frac{2\Psi d}{N_0} p(t, y); \tag{13}$$

$\Psi = 3/B - \Lambda$. The boundary leakage condition at $y = \pm d$ (the upper and lower surface of the beam) is

$$\frac{\partial P}{\partial Y}(\tau, \pm 1) = \mp \eta P(\tau, \pm 1) \tag{14}$$

where η is the leakage coefficient, which is a measure of how free is the pore fluid permitted to leak through the upper and lower surfaces of the beam. $\eta = \infty$ means there is no resistance whatsoever to the fluid leakage (equivalently, $P(\tau, \mp 1) = 0$), and $\eta = 0$ means there is no leakage whatsoever (equivalently, $\partial P/\partial Y = 0$ at $Y = \mp 1$). Notice that in this formulation:

(1) The upper and lower surface have the same leakage coefficient, hence if the bending moment vanishes, $M_z = 0$ ($M = 0$, pure compression case), the problem is symmetric with respect to the midplane $Y = 0$. Thus the solution to the pore fluid pressure is also symmetric to $Y = 0$ plane, or $\partial P/\partial Y = 0$ at $Y = 0$. This means that in the pure compression loading scenario, the midplane of the beam is also a no-leakage plane.
(2) The solution satisfies both the mass conservation equation, eqn (11), and the compatibility equation, eqn (8).

As we discussed in the Introduction, calculation of the bone fluid pressure in the osteonal cortical bone at the lacunar–canalicular level is reduced to the problem of calculating it in an axisymmetric, cylindrical bony substructure called an osteon subjected to axial compression. Ideally, the exterior boundary of an osteon (cement line) is a no-leakage boundary. In contrast, there seems to be a direct connection between the central lumen of

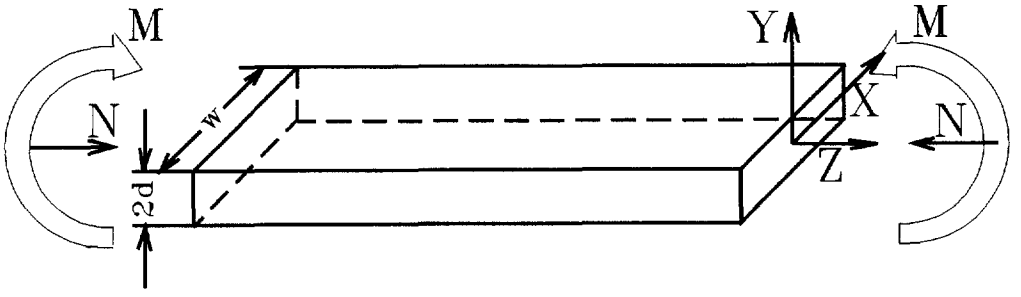

Fig. 1. The beam and the coordinate system employed.

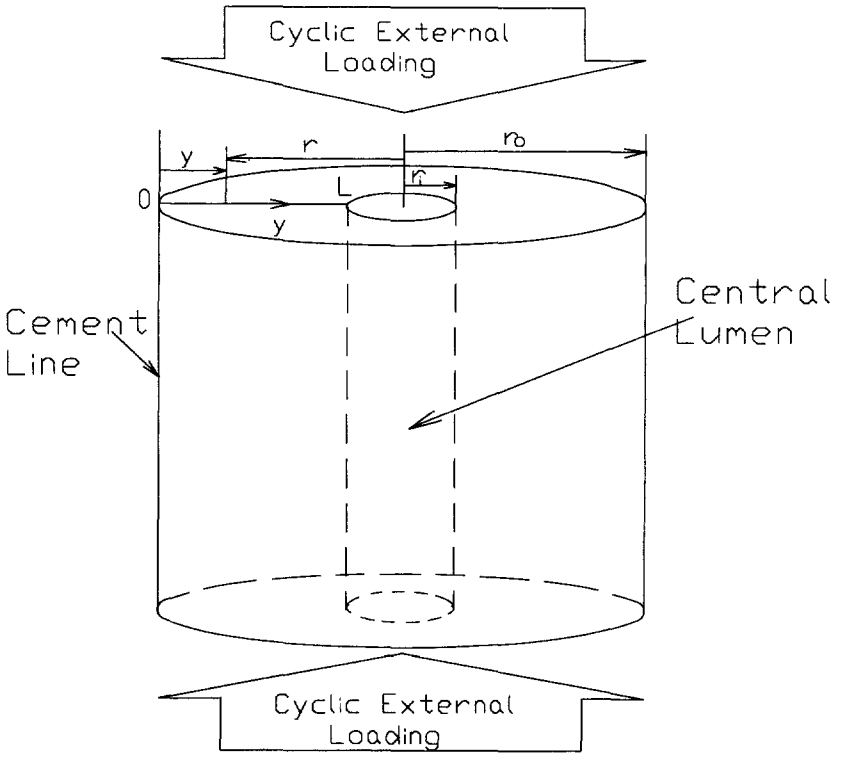

Fig. 2. The osteon and the coordinate system employed.

an osteon and the canaliculi leading to it (Kelly, 1983). This suggests a free leakage condition along the lumenal surface. Recall in the beam configuration we discussed in the above paragraph, we have the same leakage scenario along the half-thickness of a purely compressed beam with $\eta = \infty$. Harrigan and Hamilton (1993) proposed using the solution of pore fluid pressure in a poroelastic beam (with a thickness twice the annular thickness of an osteon) to simulate that generated in an osteon under the same compressional loading (beam analogy). This beam analogy (Fig. 3) is also used in Zhang *et al.* (1997) to quantify the load-induced pore fluid pressure and strain generated streaming potential (SGP) along the annular thickness of an osteon, using the solution from Zhang and Cowin (1994).

Single osteon solution

Zeng *et al.* (1994) derived a solution of the bone fluid pressure in a single annular cylindrical osteon under an oscillatory compression (Fig. 2) based on a poroelastic approach and the following two assumptions:

(1) the uniform total axial stress is given by $T_z = -T_0 \sin \omega t$ for every point (all other stresses are neglected);
(2) the influence of the compatibility equation, eqn (8), is small and hence negligible compared with the mass conservation equation, eqn (11).

T_0 is the amplitude of the axial total stress T_z and ω is its angular frequency. In the single osteon shown in Fig. 2, r is the local osteonal radius, measured from $r = r_i$ at the wall of the osteonal lumen to $r = r_0$ at the cement line, $r_i < r < r_0$. $L = r_0 - r_i$ is the annular thickness of the osteon. If we choose the following nondimensionalization

$$R \equiv \frac{r}{L}, \quad L = r_0 - r_i, \quad R_0 = \frac{r_0}{L}, \quad R_i = \frac{r_i}{L},$$

$$t_p^* \equiv \frac{t}{t_p}, \quad t_p = \frac{L^2}{c}, \quad T \equiv \frac{\omega L^2}{c}, \quad P(t_p^*, R) \equiv \frac{\Psi}{T_0} p(t, r), \tag{15}$$

where t_p is called the pore fluid pressure relaxation time across distance L (Zhang *et al.*, 1997), the osteonal solution should be analogous to the beam solution if we let $d = L$ and $N_0 = 2dT_0$ in eqn (13) and assuming the same material properties for both the beam and the osteon. This is so because now the two loading cases have the same material, same leakage condition, same diffusion distance (distance from the no-leakage point to the free leakage point), and under the same extent of nominal axial loading. In terms of the configuration, the only difference is the geometry effect: one is a rectangular thin beam and the other is an axisymmetric hollow cylinder. In terms of the solving processes, the beam solution starts with a known axial external force (an integration of the axial total stress) and considers both the fluid mass conservation equation, eqn (11), and the compatibility equation, eqn (8), while the osteon solution starts with a known axial total stress for every spatial point, neglects all other stress components and considers only the fluid mass conservation equation, eqn (11). Table 1 summarizes the differences between the two approaches.

The solution for the nondimensional bone fluid pressure within an osteon, $P(t_p^*, R)$, can be rewritten in real form from eqn (19) of Zeng *et al.* (1994), as

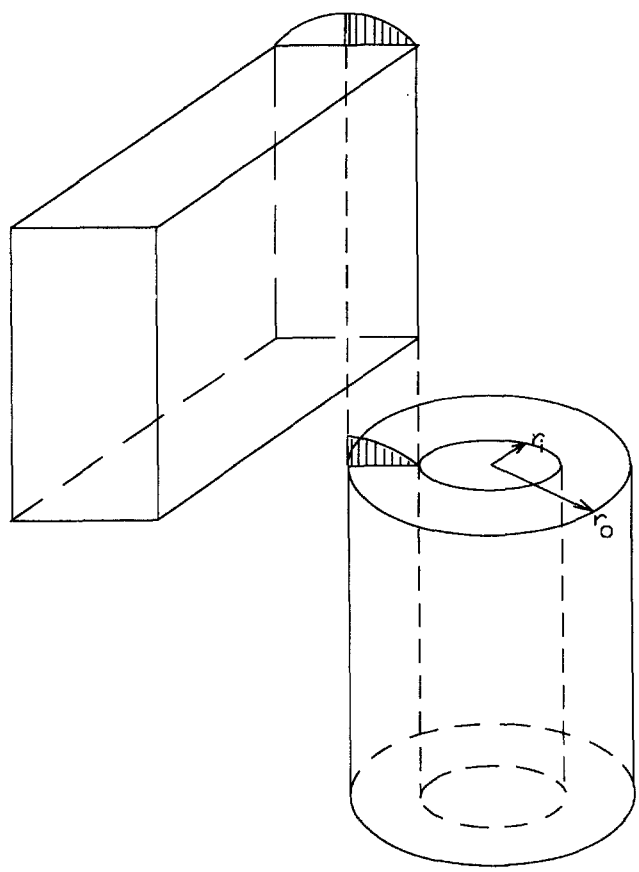

Fig. 3. The beam analogy: correspondence between the beam solution and the single osteon solution.

Table 1. Comparison between the two different approaches in solving bone fluid pressure in an osteon under axial compression

Comparison	Beam solution (Zhang and Cowin, 1994)	Single osteon solution (Zeng *et al.*, 1994)
Material properties (same)	Cortical bone matrix	Cortical bone matrix
Leakage conditions (same)	One end free leakage, other end no leakage	One end free leakage, other end no leakage
Diffusion distances (same)	$d = L$ = annular thickness of osteon	L = annular thickness of osteon
Geometries (different)	Rectangular thin beam	Axisymmetric hollow cylinder
Major assumptions (different)	Known pure axial force: $N_z = -N_0 \sin \omega t$, $M_z = 0$ One-dimensionality	Known axial total stress $T_z = -T_0 \sin \omega t$, all other stresses = 0
Set of governing equations (different)	Fluid mass conservation Compatibility equation	Fluid mass conservation only
Loading stresses (same)	$N_0/2d$	$T_0 = N_0/2d$

$$P(t_p^*, R) = \frac{\Psi}{\Psi+\Lambda}(A_{01} ber_0(\sqrt{T}R) - A_{02} bei_0(\sqrt{T}R) + B_{01} ker_0(\sqrt{T}R) - B_{02} kei_0(\sqrt{T}R)) \cos Tt_p^* - \frac{\Psi}{\Psi+\Lambda}(-1 + A_{02} ber_0(\sqrt{T}R) + A_{01} bei_0(\sqrt{T}R) + B_{02} ker_0(\sqrt{T}R) + B_{01} kei_0(\sqrt{T}R)) \sin Tt_p^*, \tag{16}$$

where

$$A_{01} = \frac{1}{\delta_1^2+\delta_2^2}(-\delta_1 ker_1(\sqrt{T}R_0) - \delta_2 kei_1(\sqrt{T}R_0)), \tag{17}$$

$$A_{02} = \frac{1}{\delta_1^2+\delta_2^2}(-\delta_1 kei_1(\sqrt{T}R_0) + \delta_2 ker_1(\sqrt{T}R_0)), \tag{18}$$

$$B_{01} = \frac{1}{\delta_1^2+\delta_2^2}(\delta_1 ber_1(\sqrt{T}R_0) + \delta_2 bei_1(\sqrt{T}R_0)), \tag{19}$$

$$B_{02} = \frac{1}{\delta_1^2+\delta_2^2}(\delta_1 bei_1(\sqrt{T}R_0) - \delta_2 ber_1(\sqrt{T}R_0)), \tag{20}$$

and

$$\delta_1 = -kei_1(\sqrt{T}R_0) ber_0(\sqrt{T}R_i) - ker_1(\sqrt{T}R_0) bei_0(\sqrt{T}R_i) + kei_0(\sqrt{T}R_i) ber_1(\sqrt{T}R_0) + ker_0(\sqrt{T}R_i) bei_1(\sqrt{T}R_0), \tag{21}$$

$$\delta_2 = ker_1(\sqrt{T}R_0) ber_0(\sqrt{T}R_i) - kei_1(\sqrt{T}R_0) bei_0(\sqrt{T}R_i) - ker_0(\sqrt{T}R_i) ber_1(\sqrt{T}R_0) + kei_0(\sqrt{T}R_i) bei_1(\sqrt{T}R_0). \tag{22}$$

ber_i, bei_i, ker_i, kei_i, $i = 0, 1$, are Kelvin functions. Λ and Ψ are nondimensional material parameters describing the porous media. For the bone matrix we find $\Lambda = 0.35$ and $\Psi = 5.3$ (Zhang and Cowin, 1994).

Comparison between the two solutions

In order to compare with the one-dimensional beam case, we introduce a spatial variable Y along the radius of an osteon, where

$$Y = 1 - \frac{r - r_i}{r_0 - r_i} = 1 - \frac{R - R_i}{R_0 - R_i}, R = (R_0 - R_i)(1 - Y) + R_i, \quad Y \in [0, 1]. \tag{23}$$

In this way we can plot $P(t_p^*, Y)$ obtained from eqn (16) and $P(\tau, Y)$ obtained from the beam analysis (Zhang and Cowin, 1994) together for comparison.

In order to characterize the geometry of an osteon, we now introduce a parameter $\delta = r_0/r_i = R_0/R_i$. δ ($\delta > 1$) is the radius ratio between the radius of the exterior rim of a hollow cylinder and that of the interior rim. A very large δ corresponds to the case when the radius of the central canal of the hollow cylinder is very small compared with its exterior radius (point hole problem). $\delta \to 1$ corresponds to the case when the radii of the two rims are so close that you can almost cut the ring open and extend it to get a rectangle. For a physiological osteon, r_i varies from 2.5–85 μm (Atkinson and Hallsworth, 1982), with a probability-weighted average (expected mean) at about 25 μm. r_0 varies from 100–150 μm (Martin and Burr, 1989) with an average at about 130 μm; we will see that the value of δ varies from 1.1–60 with a probability-weighted average (expected mean value) at about 5.2, assuming that the two radii, r_i and r_0, are two independent random values. The reasons for this independence are, first, r_i is contributed by the tunneling effort of the bone-eroding osteoclasts and r_0 by a separate group of bone-building osteoblasts. Secondly, the time lag between the initiation of tunneling by osteoclast and the initiation of refilling by osteoblasts is about 30 days (Martin and Burr, 1989).

Stress decomposition factors

Equation (5) can be rewritten as

$$T_{ij} = \sigma_{ij}^{(s)} - \zeta p \delta_{ij} = \sigma_{ij}^{(s)} + \sigma^{(f)} \delta_{ij}, \tag{24}$$

where $\sigma_{ij}^{(s)}$ are the constituent stresses on the solid phase which can be interpreted as the portion of the total stress T_{ij} that is supported by the solid part of the medium. In conventional soil mechanics, $\sigma_{ij}^{(s)}$ are known as the effective stresses (Nur and Byerlee, 1971). The constituent stress on the fluid phase is hydrostatic, so we use a single expression $\sigma^{(f)}$ to denote it. We use S_{ij}, $S_{ij}^{(s)}$ and $S^{(f)}$ to denote the nondimensionalized T_{ij}, $\sigma_{ij}^{(s)}$ and $\sigma^{(f)}$ (Zhang and Cowin, 1996).

In respect to the bone problem at hand, the axial total stress T_{33} is the dominant stress component since it is in the direction of our external loading. It is of interest to know how T_{33} is decomposed at the non-leakage point of the osteon (namely the cement line, $Y = 0$). Since T_{33}, $\sigma_{33}^{(s)}$, $\sigma^{(f)}$ are oscillatory, we can define the stress decomposition factors as

$$\beta_1 = \left(\frac{(S^{(f)})_{a\tau}}{(S_{33}^{(s)})_{a\tau}} \right)_{Y=0}, \quad \beta_2 = \left(\frac{(S^{(f)})_{a\tau}}{(S_{33})_{a\tau}} \right)_{Y=0}, \tag{25}$$

where $(\,)_{a\tau}$ is the average operator over the time period,

$$(\,)_{a\tau} = \frac{T}{2\pi} \int_0^{2\pi/T} (\,) \, \mathrm{d}\tau. \tag{26}$$

β_1, called the stress decomposition ratio, can be interpreted as the relative ratio of the two portions of the total axial stress (one is the fluid partial stress and the other is the solid partial stress). β_2, called the stress contribution factor of the bone fluid pressure, is roughly the percentage of the total axial stress that is supported by the pore fluid.

PARAMETER EVALUATION

As we mentioned before, our problem is focused on treating the cortical bone matrix as a poroelastic medium with the lacunar–canalicular level permeability. Balance between blood and the surrounding interstitial tissue's hydrostatic and oncotic (osmotic) pressures across the blood vessel wall (Starling's law) determines the bone fluid pressure in the higher level vascular porosity. Parameter evaluation of the biological systems varies greatly with specimen selection and the parameterization methodology. Detailed characterization of the poroelastic parameters of the cortical bone matrix at the lacunar–canalicular system can be found in Weinbaum *et al.* (1994), Cowin *et al.* (1995), Zhang and Cowin (1994), Zhang *et al.* (1997, 1998). Key parameter evaluation can be summarized as follows: $B = 0.53$, $\Lambda = 0.35$, $\Psi = 5.3$, $\zeta = 0.27$, $c = 3.76 \times 10^{-7}$ m^2/s, $r_i = 25$ μm (varying from 2.5–85 μm), $r_0 = 130$ μm (ranging from 100–150 μm), $\delta = 5.2$ (varying from 1.1–60) and $T_0 = 9$ MPa for 1000 microstrain oscillatory compressive loading at 1 Hz.

RESULTS

In order to summarize our results, we can write the pore fluid pressure calculated from the single osteon approach as

$$P(t_p^*, Y, \delta) = P_{amp}(T, Y, \delta)\sin(Tt_p^* - \alpha), \quad \alpha = \alpha(T, Y, \delta), \tag{27}$$

and that from the beam approach as

$$P(\tau, Y) = P_{amp}(T, Y)\sin(T\tau - \alpha), \quad \alpha = \alpha(T, Y). \tag{28}$$

Figure 4 shows the comparison of the behavior of the magnitude of the load-induced fluid pressure at the maximally pressurized point $P_{amp}(T, 0, \delta)$ or $P_{amp}(T, 0)$ (or no-leakage point: midplane of the beam in the beam approach, cement line in the single osteon approach) as a function of the nondimensional frequency T calculated from the analytical solutions based on the beam approach and the single osteon approach. We choose different values of δ in the single osteon approach to show the dependence of the solution on the

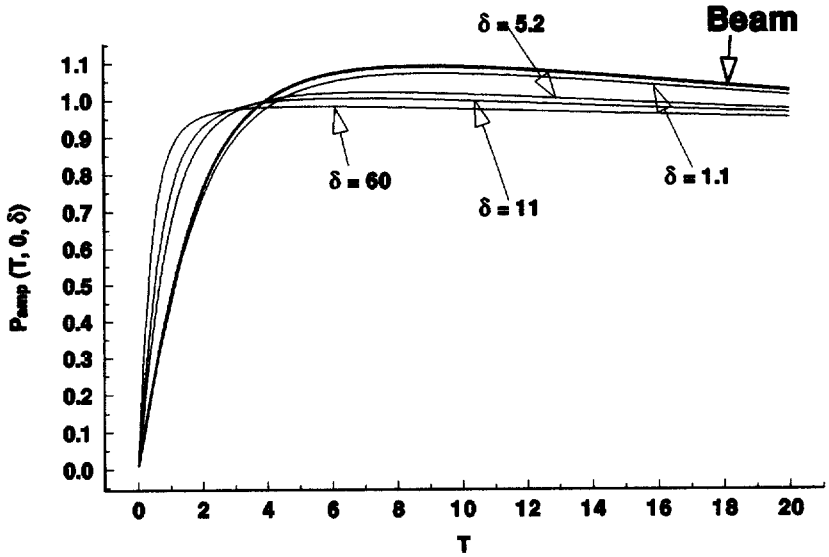

Fig. 4. Dependence of the amplitude of the nondimensional load-induced bone fluid pressure at the cement line, $P_{amp}(T, 0, \delta)$, on the nondimensional frequency T and the exterior-to-interior radius ratio δ.

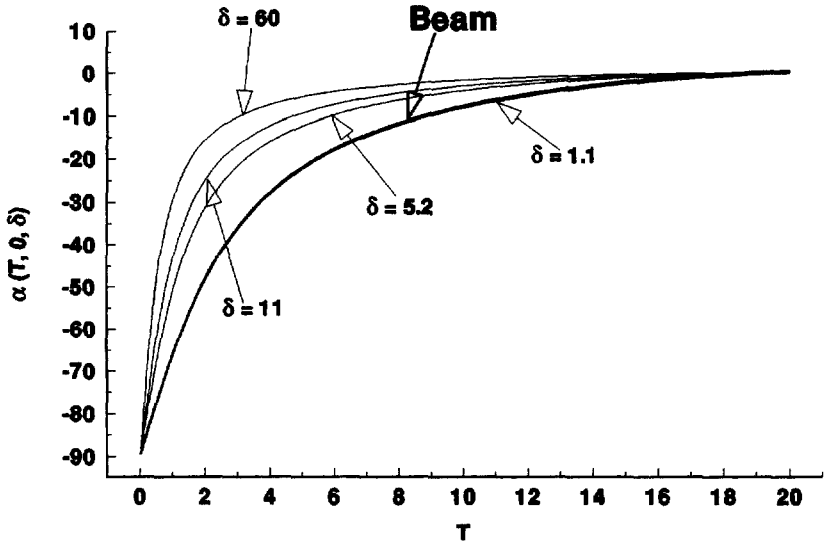

Fig. 5. Dependence of the phase angle of the load-induced bone fluid pressure at the cement line, $\alpha(T, 0, \delta)$, on the nondimensional frequency T and the exterior-to-interior radius ratio δ.

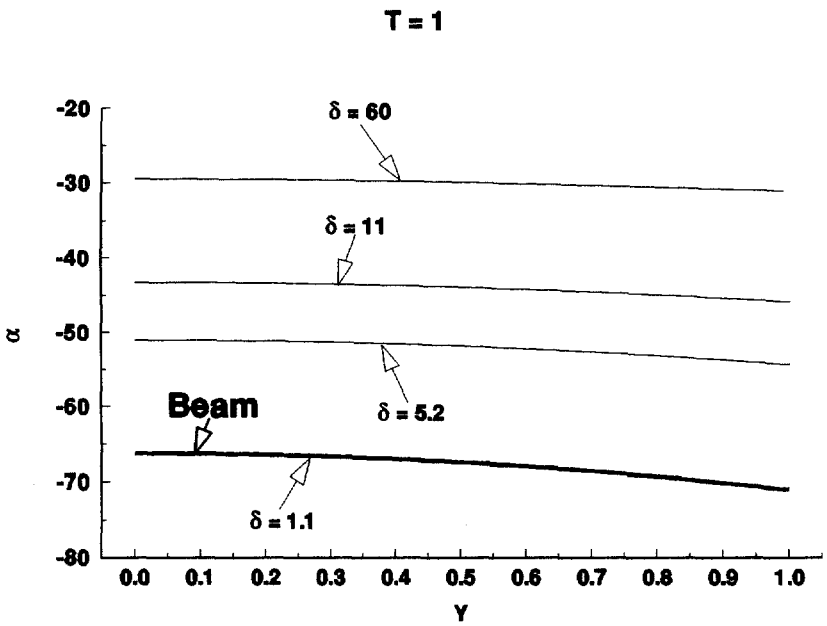

Fig. 6. Spatial profiles of the phase angle of the load-induced bone fluid pressure when the nondimensional frequency $T = 1$ (5 Hz), $\alpha(1, Y, \delta)$, for different values of the exterior-to-interior radius ratio δ.

geometry of the hollow cylinder. Figure 5 shows the corresponding behavior of the phase angle of the fluid pressure at the no-leakage point, $\alpha(T, 0, \delta)$ or $\alpha(T, 0)$.

Figure 6 shows how the phase angles, $\alpha(T, Y, \delta)$ and $\alpha(T, Y)$, of the load-induced fluid pressure varies with the spatial coordinate Y for different geometries and a representative nondimensional frequency $T = 1$. The figure shows that the phase angle is essentially a constant with respect to space in each geometry. In other words, at each spatial point along the osteonal radius, the load-induced bone fluid pressure will attain its maximum value at approximately the same time, even though each spatial point is entitled to have its own phase of oscillation. What this means is that $P_{amp}(T, Y, \delta)$ and $P_{amp}(T, Y)$ profiles plotted

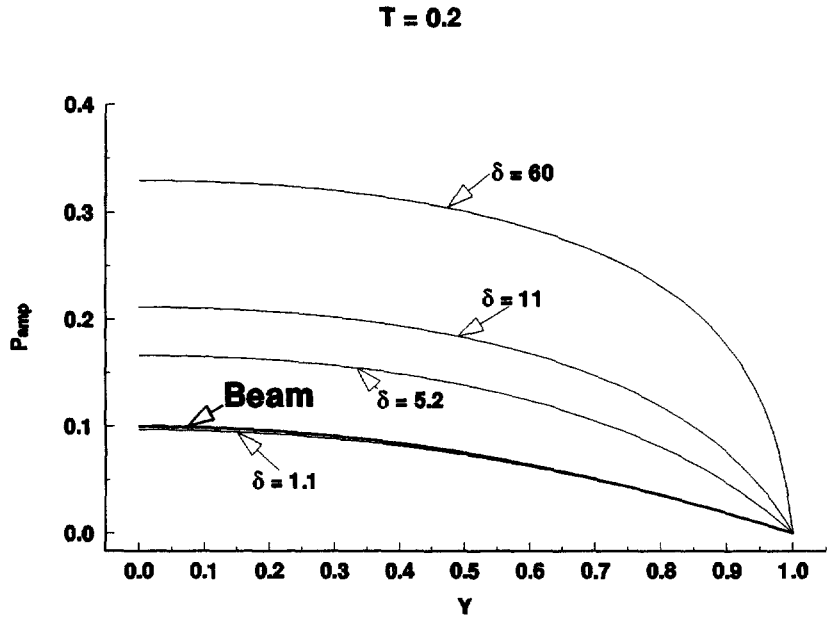

Fig. 7. Spatial profiles of the amplitude of the load-induced bone fluid pressure when the non-dimensional frequency $T = 0.2$ (1 Hz), $P_{amp}(0.2, Y, \delta)$, for different values of the exterior-to-interior radius ratio δ.

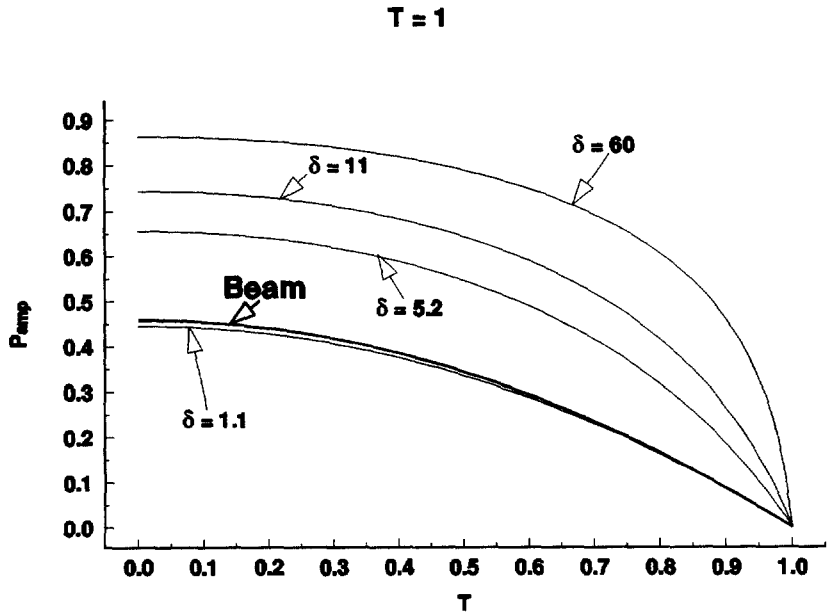

Fig. 8. Spatial profiles of the amplitude of the load-induced bone fluid pressure when the non-dimensional frequency $T = 1$ (5 Hz), $P_{amp}(1, Y, \delta)$, for different values of the exterior-to-interior radius ratio δ.

in Fig. 7 are very similar to the real pressure profiles at the time $Y = 0$ point reaches the maximum.

Figure 10 shows how the frequency-dependent behavior of the stress decomposition ratio β_1 of an osteon, defined in eqn (25), varies as a function of the geometric factor δ. The same decomposition ratio is also plotted based on the beam solution (thick curve). As a reference, the stress contribution factor of the pore fluid pressure, β_2, is also plotted for the beam solution. Correspondent β_2 curves derived from the osteon solution are not

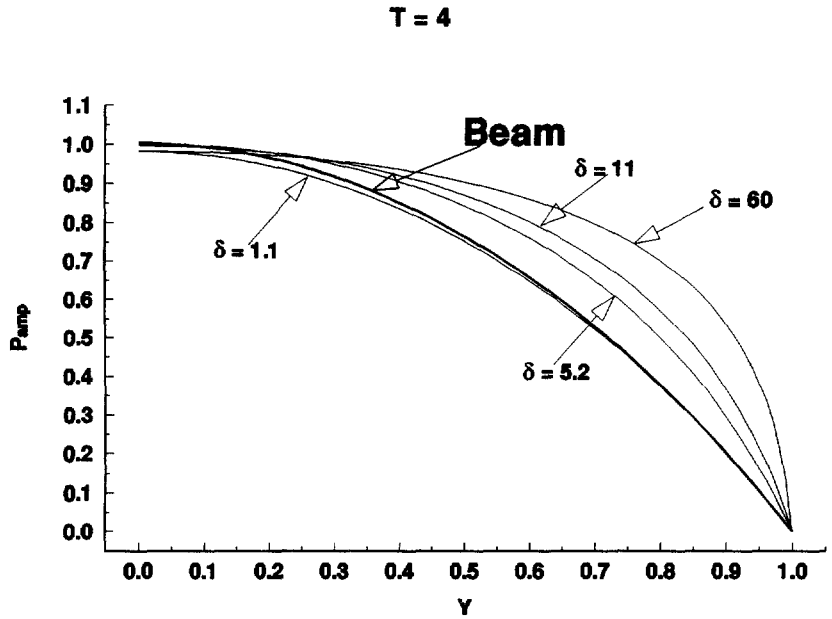

Fig. 9. Spatial profiles of the amplitude of the load-induced bone fluid pressure when the non-dimensional frequency $T = 4$ (20 Hz), $P_{amp}(4, Y, \delta)$, for different values of the exterior-to-interior radius ratio δ.

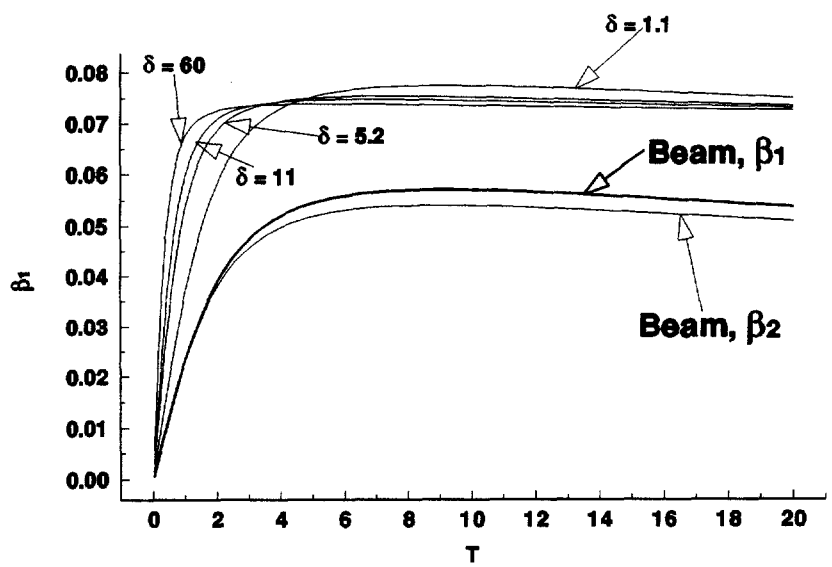

Fig. 10. Frequency-dependent behavior of the stress decomposition ratio of the axial total stress defined in eqn (25), β_1. The curve for the bone fluid stress contribution factor, β_2, derived from the beam solution is also included for reference.

plotted, but their relative behavior with respect to their respective β_1 curves are similar to that between the β_2 and β_1 curves for the beam solution (data not shown).

DISCUSSION

We want to point out that even though we are discussing the solutions in the context of a single osteon within a compact bone matrix, the same solution can also be used to a long bone under uniaxial compression if we want to calculate the load-induced hydrostatic pressure in the vascular porosity, since a long bone section can also be idealized as an

annular cylindrical tube. It has been shown that the periosteum is a layer of relatively impermeable membrane and the endosteal surface is perforated with centrifugal terminal blood vessels branching out from the main nutrient vessels in the marrow cavity (Brookes, 1971; Kelly, 1983), hence the same leakage conditions that apply to a single osteon also apply to a long bone section. However, the fluid pressure relaxation time in the vascular porosity is several orders of magnitude lower than that in the lacunar–canalicular space (see below). In the soil or rock mechanics context, the solution presented here may also be useful in calculating fluid movement around a borehole or a well.

Relaxation times of the three levels of porosity

The pore fluid pressure relaxation time t_p of a poroelastic solid cross a distance L can be defined as $t_p = L^2/c$ [eqn(15)], c is the diffusion constant defined in eqn (12). In cortical bone, we have three levels of porosity, so theoretically we should have three different values of diffusion constants (with possible coupling between them) for each of them. From eqn (12), we see that at each level, the diffusion constant c is equal to the permeability κ at that level times a factor that is related to the stiffness, the compressibility, and the solid–fluid interaction of the poroelastic solid at that level. At the first level of analysis, let's assume that this factor is comparable for these three levels and focus our attention on the permeability.

If all the pores in the three levels of porosity are free from soft tissues, the permeability is about proportional to the square of the pore size. Since the pore size ratios of the three levels of porosity (crystal level, lacunar–canalicular level and vascular level) are about $1:10:2500$, the permeability ratios are about $1:10^2:10^6$ (100 A : 0.2 μ : 50 μ, Atkinson and Hallsworth, 1982; Holmes *et al.*, 1964). However, in Weinbaum *et al.* (1994), and later papers, we postulate that there is a glycocalyx (GAG) cell coat on the plasma membrane that fills the lacunar–canalicular space. The existence of this extracellular matrix will decrease the permeability of the lacunar–canalicular level by about two orders of magnitude. Hence, the permeability ratios of these three levels of porosity could be $1:1:10^6$. However, Neuman and Neuman (1958) pointed out that bone water at the crystal level is largely bound to the crystal surface by a very strong electric attraction, hence not likely free to move. (If this is true, the permeability ratios will be $0:1:10^6$.) Based on this, in this paper we only consider the load-induced bone fluid in the lacunar–canalicular porosity since the vascular porosity serves as a low-pressure bone fluid reservoir.

Weinbaum *et al.* (1994) give a detailed description on how to evaluate the permeability of the lacunar–canalicular porosity of the cortical bone matrix based on a three-step hierarchical model. Base on this model, Zhang *et al.* (1997) estimated that the diffusion constant $c = \kappa$ (25.56 GPa) $= 3.76 \times 10^{-7}$ m^2/s. (Here $\kappa = k/\mu$, $k = 1.471 \times 10^{-20}$ m^2, if $\mu = 10^{-3}$ Pa s.) Across a diffusion distance of $L = 100$ μm (typical annular thickness of an osteon), the ideal pore pressure relaxation time $t_p = L^2/c = 2.9 \times 10^{-2}$ s. Hence a 1 Hz loading will correspond to a nondimensional frequency $T = 0.2$ [eqn (13) or (15)].

Influence of the geometry factor

The influence of the geometry factor represented by the exterior-to-interior radius ratio δ of the annular cylinder can be best interpreted from Figs 4, 5, and 7. Figure 4 shows how the amplitude of the load-induced pore fluid pressure at the no-leakage location (exterior boundary of the osteon or the midplane of the beam), $P_{amp}(T, 0, \delta)$ or $P_{amp}(T, 0)$ in eqn (24) or (25), changes with frequency T. Each curve is plotted for one value of the geometry factor δ, $\delta = 1.1$, 5.2, 11, 60. As we recall, δ close to 1.0 corresponds to a thin-walled annular cylinder and a very large δ corresponds to an almost solid cylinder with a thin central hole. For a physiological osteon, δ varies from 1.1–60 with an expected mean value of 5.2. As δ approaches one, the osteon curves approach the beam curve. In Fig. 4, each curve shows a typical behavior of a high-pass filter with respect to the nondimensional loading frequency T for each value of δ. A high-pass filter is a concept of electronics which means a device that lets through the higher-frequency components (with respect to a threshold frequency) of an incoming signal and filters out the lower-frequency components. This threshold frequency is also called the corner frequency, or cutoff frequency. A low-pass filter is a device that does the opposite.

We have shown in previous papers (Zhang *et al.*, 1997, 1998) that in transferring the mechanical loading signal into its induced pore fluid pressure signal through the poroelastic bone matrix, the ideal corner frequency for the high-pass filter cascade is related to t_p^{-1}, where t_p is the pore fluid relaxation time across a half beam thickness L, $t_p = L^2/c$. Figure 4 shows that for an annular cylinder such as an osteon, the corner frequency is also related to the geometry factor δ, since the corner frequency decreases as δ increases. The reason for this is that as $\delta = r_0/r_i$ increases while $L = r_0 - r_i$ remains constant, the specific leakage surface area (defined by $2\pi r_i/\pi(r_0^2 - r_i^2) = 2/L(\delta+1)$) decreases, hence the bone fluid pressure becomes more and more difficult to relax. Hence the corner frequency for the pore fluid pressure decreases. Another way of interpreting this is by defining an equivalent diffusion distance. Even though the distance between the no-leakage point and the free-leakage point is still L, due to the competing effect of the same amount of fluid running out of smaller outlet area, the equivalent diffusion distance (probably related to δ) is somewhat larger than L. In the ideal beam case, the corner frequency is close to $T = 6$ (which corresponds to $t_p^{-1} = 30$ Hz).

Figure 5 shows the corresponding frequency-dependent behavior of the phase of the load-induced pore fluid pressure at the no-leakage point (cement line and the midplane of the beam), $\alpha(T, 0, \delta)$ and $\alpha(T, 0)$ in eqns (24), (25). Similar to Fig. 4, as δ approaches 1, the response of the osteon approaches the response of the beam. As δ increases, the phase of the load-induced pore fluid pressure keeps pace with the external load more quickly as the frequency increases.

Figure 7 shows the amplitude profiles of the load-induced pore fluid pressure for one fixed value of the nondimensional frequency $T = 0.2$, $P_{amp}(0.2, Y, \delta)$ and $P_{amp}(0.2, Y)$. Again, we can see that as δ approaches 1, the osteon profiles approach those of the beam. For a very large δ, P_{amp} not only operates at a higher magnitude but also has a quite different profile compared with that of the beam. For example, at $\delta = 60$, most of the pressure drop occurs near the free-leakage boundary $Y = 1$, while in the beam profile the pore fluid pressure drops almost linearly across the thickness. Comparing Figs 7–9 plotted for different frequencies, $T = 0.2$, 1, and 4, we can see that the difference of the end values (i.e. at $Y = 0$) between the beam solution and the large-δ single osteon solution decreases as T increases. At $T = 4$, the end value of the beam solution at $Y = 0$ and the single osteon solution at $y = 0$ at all values of δ are about the same. However, the differences in the profile shape for different values of δ still persist.

Magnitude of the load-induced bone fluid pressure and pressure differences

Bone fluid movement is driven by spatial bone fluid pressure differences. There are two major sources of pressure drop in bone: the one generated by blood pressure and the one generated by external loading. Since static load cannot produce a sustained bone fluid pressure due to the bone fluid pressure relaxation, only dynamic loads are important in this context.

From eqns (13) and (15), we can see that the dimensional pressure p equals the nondimensional pressure P times T_0/Ψ, where T_0 is the amplitude of the externally applied cyclic axial total stress and Ψ is a material constant, $\Psi = 5.3$ (Zhang and Cowin, 1994). The peak local strain magnitude measured in a variety of bones in a wide range of animals during the extremes of functional activity is similar. This range is from 2500–3500 μstrain. However, the local strain magnitude in the majority of bone tissue is 1000 μstrain or less (Rubin and McLeod, 1995). Hence we choose a strain level of 1000 μstrain as the yardstick for our parameter evaluation. Since the axial Young's modulus for bone is about 18 GPa (Cowin, 1989), the axial stress level is about 18 MPa. In other words, the cyclic stress varies from 0–18 MPa under physiological loading, hence one-half of that range is $T_0 = 9$ MPa. (Here we shift the range of external stress from 0 to 18 MPa to -9 MPa to 9 MPa, to be consistent with a sinusoidal external loading.) In humans, this level of stress occurs in a femur under typical walking conditions at a frequency of 1 Hz. The maximum compressive stress experienced by the human femur (located around the midpoint of the femur at the medial side) during walking is about 13.52 MPa (Koch, 1917). Hence, in this loading scenario, $T_0/\Psi = 1.7$ MPa.

The value Ψ is a material constant that is, most importantly, a function of the ratio between the compressibility (bulk modulus) of the bone fluid phase and that of the solid phase in a poroelastic medium. Physically Ψ represents the share of load that is assigned to the fluid phase. In an idealized case when the poroelastic solid is under hydrostatic compression, the share of loading is assigned to each phase based on their compressibility (bulk modulus) ratio. A pore fluid of lower compressibility (higher bulk modulus) is expected to share more of the load than that of a higher one. In the case of bone, the bulk modulus of the solid matrix is about seven times larger than that of the bone fluid (Zhang and Cowin, 1994).

From Fig. 7 (at $T = 0.2$, 1 Hz), we can see that for a typical osteon ($\delta = 5.2$) the maximum bone fluid pressure generated at the cement line is about 0.16×1.7 MPa $= 0.27$ MPa (about 2.7 atm or 1852 mmHg). Comparing the two curves for $\delta = 5.2$ in Fig. 9 (for 20 Hz) and Fig. 7 (for 1 Hz), we can see that at $Y = 0$ (cement line), the load-induced nondimensional pressure magnitude P_{amp} at 20 Hz is six folds larger than that at 1 Hz. This tells us if we are applying a 20 Hz oscillatory load T_0 (20 Hz) that is six folds lower than a 1 Hz load T_0 (1 Hz), it will generate a same level of bone fluid pressure in an osteon. This suggests that low-amplitude, high-frequency (15–30 Hz) loading such as that contributed by muscle contraction is also important to bone fluid motivation and other bone fluid related mechanisms.

Brookes (1971) estimated that the periosteal circulation is a low-pressure system similar to that of the skin, with an intracapillary pressure at the periosteal surface of about 15 mmHg. At the endosteal surface, the intravascular pressure is of the order of 60 mmHg. The pressure gradient across the cortical capillaries is therefore centrifugal, and is the principal factor maintaining blood flow across the cortex of the diaphysis. Based on this estimate, the total blood pressure difference across the cortex of a long bone is about 45 mm Hg. Since the capillary pressure within the osteonal lumen is probably below 15 mm Hg, during normal physiological functioning, the load-induced bone fluid pressure difference across the radius of a single osteon is 40 times larger than the blood pressure difference across the whole cortex. This means that in a load-carrying bone, bone fluid movement in the lacunar–canalicular space is dominantly driven by the external mechanical loading instead of by the blood pressure difference. Since bone fluid movement at this level is very important to the normal metabolism of the osteocytes embedded in the mineralized matrix, our analysis might explain why live bone deteriorates so quickly after its loading level decreases.

Stress-sharing capacity of the bone fluid pressure

As we have hypothesized, the bone fluid filled lacunar–canalicular space takes only 5% of the bone matrix volume (porosity = 0.05). As shown in Fig. 10, the stress contribution factor of the load-induced bone fluid pressure calculated for the axial total stress at the no-leakage midplane of the beam, β_2, attains a plateau of 0.05 for $T > 6$. As we discussed in our previous papers (Zhang and Cowin, 1994, 1996), the coincidence of this plateau value of β_2 and the value of porosity does not seem to be accidental. At high loading frequency the pore fluid pressure does not have time to relax, hence the fluid phase deforms as an integrated part of the solid matrix, and thus the total stress is shared between the solid and fluid phases in accordance with their volume fractions.

It is of interest to note that the curves plotted in Fig. 10 look very similar to the curves in Fig. 4. This is understandable since the solid partial stress is the dominant stress component in the axial total stress. Since the stresses are nondimensionalized with respect to the applied external stress [eqns (13), (15)], approximately speaking what are plotted in Fig. 10 are just those in Fig. 4 reduced by a constant factor (about 0.1). However, there are some small differences. Notice in Fig. 4, as δ approaches 1, the curves obtained from the single osteon solution approach the curve obtained from the beam solution. This is not true in Fig. 10. There is a significant discrepancy between the β_1 curves obtained from the single osteon solution and from the beam solution even as δ approaches 1. The cause for this could be a combination of the differences between these two solutions summarized in Table 1. More specifically, the following two reasons may be the most significant:

(1) In the single osteon solution the axial stress is assumed to be known, and the other two total stress components (in the radial and hoop directions) are assumed to be zero. However, in the case of the beam solution the total stresses are obtained as solutions of the governing field equations. This could cause some discrepancy between the calculated stress decomposition factors based on these two different approaches.
(2) In the single osteon solution, only the fluid mass conservation equation is considered, while in the beam solution, both this equation and the stress compatibility equations are considered.

These two differences in methodology do not lead to a significant difference in behavior between the δ-near-1 single osteon solution and the beam solution as depicted in Figs 4–9. This tells us what is neglected in the single osteon approach is probably minor, at least for the case of bone which has a very low porosity (5%) and a very stiff solid matrix. But the differences mentioned as points (1) and (2) above can be demonstrated in the behavior of the more subtle quantities such as β_1 or β_2 defined in eqn (25), Fig. 10. However, the cause for the discrepancy shown in Fig. 10 could be a combination of (1) and (2), hence it is difficult to distinguish between these two effects.

Finally, it is interesting to point out that for both the single osteon and beam solutions we find that $\beta_2 \approx \beta_1/(1+\beta_1)$. Only the β_2 curve for the beam solution is plotted in Fig. 10. This relationship between β_2 and β_1 can be derived from our definition of the stress decomposition factors in eqn (25).

CONCLUSION

Under physiological functioning, the load-induced bone fluid pressure in the lacunar–canalicular porosity of a cortical bone matrix of a typical load-bearing bone is at least 40 times larger than that generated by the blood pressure difference. Hence the fluid movement in this level is dominantly driven by the external loading, instead of by the blood pressure difference.

In calculating the bone fluid pressure at the lacunar–canalicular level in an osteon, the efficacy of using the beam analogy depends on both the loading frequency and the geometry factor δ, which is the exterior to interior radius ratio of the osteon.

When δ is close to one, the beam analogy can serve a very good approximation to the solution for the annular cylindrical osteon in terms of matching both the end values and the detailed spatial profiles. In terms of calculating the stress-sharing characteristics between the solid and fluid phase, irreconcilable differences occur between the beam solution and the single osteon solution even as δ approaches 1. This may be caused by the differences in methodology between these two approaches.

When δ is very large compared to one, the beam analogy is a bad analogy in the low loading frequency range (below 20 Hz), within which the geometry effect of fluid leakage is significant. In the high loading frequency range (larger than 20 Hz), the beam analogy can provide good estimation to the end values of the bone fluid pressure across the annular thickness of an osteon, but fails to predict the detailed spatial profiles associated with large δ values.

Acknowledgement—This work was supported by NIH Grant IR01AR44211-01 and the PSC-CUNY Research Award Program of the City University of New York.

REFERENCES

Atkinson, P. J. and Hallsworth, A. S. (1982) The spatial structure of bone. *Progress in Anatomy*, ed. R. J. Harrison and V. Navaratnam, vol. 2, pp. 179–199. Cambridge University Press, U.K.

Brookes, M. (1971) *The Blood Supply of Bone, An Approach to Bone Biology*, p. 199. Appleton-Century-Crofts, New York.

Cooper, R. R., Milgram, J. W. and Robinson, R. A. (1966) Morphology of the osteon: an electron microscopic study. *J. Bone Jt. Surg. Am.* **48**, 1239–1277.

Cowin, S. C. (1989) The mechanical properties of cortical bone tissue, *Bone Mechanics*, ed. S. C. Cowin, pp. 97–127. CRC Press.

Harrigan, T. P. and Hamilton, J.J. (1993) Bone strain sensation via transmembrane potential changes in surface osteoblasts: loading rate and microstructural implications. *Journal of Biomechanics* **26,** 183–200.

Holmes, J. M., Davies, D. H., Meath, W. J. and Beebe, R. A. (1964) Gas adsorption and surface structure of bone mineral. *Biochemistry* **3,** 2019–2024.

Kelly, P. J. (1983) Pathways of transport in bone. *Handbook of Physiology*, Vol. III, pp. 371–396. Am. Physiol. Soc., Bethesda.

Koch, J. C. (1917) The laws of bone architecture. *Am. J. Anat.* **21**(2), p. 243.

Levick, J. R. (1991) Capillary filtration-absorption balance reconsidered in light of dynamic extravascular factors. *Exp. Physiol.* **76,** 825–857.

Martin, R. B. and Burr, D. B. (1989) *Structure, Function, and Adaptation of Compact Bone*, p. 30. Raven Press, New York.

Neuman, W. F. and Neuman, M. W. (1958) *The Chemical Dynamics of Bone*. University of Chicago Press, Chicago.

Nur, A. and Byerlee, J. D. (1971) An exact effective stress law for elastic deformation of rock with fluids. *J. Geophys. Res.* **76**(26), 6414–6419.

Rice, J. R. and Cleary, M. P. (1976) Some basic stress diffusion solutions for fluid-saturated elastic porous media with compressible constituents. *Rev. Geophys. Space Phys.* **14,** 227–241.

Rubin, C. T. and McLeod, K. J. (1995) Endogenous control of bone morphology via frequency specific, low magnitude functional strain. *Bone Structure and Remodeling*, ed. A. Odgaard and H. Weinans, Recent Advances in Human Biology Series, Vol. 2, World Scientific, pp. 79–90.

Rudnicki, J. W. (1985) Effect of pore fluid diffusion on deformation and failure of rock. *Mechanics of Geomaterials*, ed. Z. Bazant, pp. 315–347. John Wiley and Sons Ltd.

Starkebaum, W., Pollack, S. R. and Korostoff, E. (1979) Microelectrode studies of stress-generated potentials in four-point bending of bone. *J. of Biomed. Mat. Res.* **13,** 729–751.

Weinbaum, S., Cowin, S. C. and Zeng, Y. (1994) Excitation of osteocytes by mechanical loading-induced bone fluid shear stresses. *Journal of Biomechanics* **27**(3), 339–360.

Zeng, Y., Cowin, S. C. and Weinbaum, S. (1994) A fiber matrix model for fluid flow and streaming potentials in the canaliculi of an osteon. *Ann. Biomed. Eng.* **22,** 280–292.

Zhang, D. and Cowin, S. C. (1994) Oscillatory bending of a poroelastic beam. *Journal of the Mechanics and Physics of Solids* **42**(10), 1575–1599.

Zhang, D. and Cowin, S. C. (1996) Load carrying capacity of the pore pressure in a poroelastic beam subject to oscillatory excitation. *Mechanics of Poroelastic Media*, ed. A. P. S. Selvadurai, Wolters Kluwer Academic Publishers, Solid Mechanics and Its application Series, vol. 35, pp. 273–298.

Zhang, D., Cowin, S. C. and Weinbaum, S. (1997) Electrical signal transmission and gap junction regulation in a bone cell network: a cable model for an osteon. *Ann. Biomed. Eng.* **25,** 357–374.

Zhang, D., Weinbaum, S. and Cowin, S. C. (1998) Electrical signal transmission in a bone cell network: the influence of a discrete gap junction. *Ann. Biomed. Eng.* **26,** 644–659.